optica

Circumventing the optical diffraction limit with customized speckles

Nicholas Bender,[1] Mengyuan Sun,[2] Hasan Yilmaz,[1] Joerg Bewersdorf,[3,4] and Hui Cao[1,*]

[1]Department of Applied Physics, Yale University, New Haven, Connecticut 06520, USA
[2]Department of Molecular Biophysics and Biochemistry, Yale University, New Haven, Connecticut 06520, USA
[3]Department of Cell Biology, Yale University School of Medicine, New Haven, Connecticut 06520, USA
[4]Department of Biomedical Engineering, Yale University, Yale University, New Haven, Connecticut 06520, USA
*Corresponding author: hui.cao@yale.edu

Received 25 September 2020; revised 20 November 2020; accepted 23 November 2020 (Doc. ID 411007); published 22 January 2021

Speckle patterns have been used widely in imaging techniques such as ghost imaging, dynamic speckle illumination microscopy, structured illumination microscopy, and photoacoustic fluctuation imaging. Recent advances in the ability to control the statistical properties of speckles has enabled the customization of speckle patterns for specific imaging applications. In this work, we design and create special speckle patterns for parallelized nonlinear pattern-illumination microscopy based on fluorescence photoswitching. We present a proof-of-principle experimental demonstration where we obtain a spatial resolution three times higher than the diffraction limit of the illumination optics in our setup. Furthermore, we show that tailored speckles vastly outperform standard speckles. Our work establishes that customized speckles are a potent tool in parallelized super-resolution microscopy.

https://doi.org/10.1364/OPTICA.411007

1. INTRODUCTION

When a large number of random partial waves interfere, an irregular pattern of speckled grains, commonly called a speckle pattern or speckles, is created. If the amplitudes and phases of the partial waves independently vary—and the phases are uniformly distributed over a range of 2π—the speckle pattern is fully developed [1–3]. Most speckle patterns satisfy Rayleigh statistics, wherein the joint probability distribution of the complex field is circular Gaussian, and the probability density function (PDF) of the intensity is a negative exponential [1,2]. The topology of a Rayleigh speckle pattern can be characterized as an irregular and interconnected low-intensity web with isolated high-intensity islands. While the bright speckle grains are all relatively isometric and isotropic [3], the dark regions surrounding optical vortices are anisotropic [4–7]. In various imaging and metrology techniques, speckle patterns are used to illuminate samples to improve precision, resolution, visibility, and sectioning while simultaneously providing a wide field of view [8–21].

In fluorescence microscopy, a sub-diffraction-limited resolution can be obtained with saturable structured illumination techniques. Examples include stimulated emission depletion (STED) microscopy [22,23], ground state depletion (GSD) microscopy [24], and reversible saturable optical fluorescence transitions (RESOLFT) [25–27]. Generally, these techniques rely on spatially modulating the illumination intensity to toggle fluorescence on and off in a spatially selective manner. For example, in RESOLFT, a doughnut-shaped optical beam photoconverts all fluorophores in a region of a sample except those close to the vortex center, and therefore fluorescence is emitted only from a sub-diffraction-sized region. Usually, point scanning of the doughnut beam is required to construct an image, which can be very time consuming. Recently, this process has been parallelized using either a one-dimensional (1D) standing wave pattern [28] or a two-dimensional (2D) lattice of doughnuts [27]. The first method involves rotating or translating the illumination pattern, and as a result, post-processing is required for 2D super-resolution since each individual pattern improves the resolution in only one direction. In the second method, two incoherently superimposed orthogonal standing waves create a square lattice of intensity minima, but axial uniformity of the intensity pattern hinders optical sectioning. One way to circumvent this issue is to use the optical vortices in a speckle pattern as the nonlinear structured illumination pattern [29]. Because fully developed speckle patterns rapidly and non-repeatably change along the axial direction, they can be used to obtain a three-dimensional (3D) super-resolution image [30]. In this context, speckles are advantageous because they are robust to optical distortions/aberrations while simultaneously enabling 3D super-resolution [9–21,30,31]. The problem with using Rayleigh speckles, however, is that the anisotropic and strongly fluctuating shapes of their optical vortices leads to non-isotropic and non-uniform improvements in the spatial resolution.

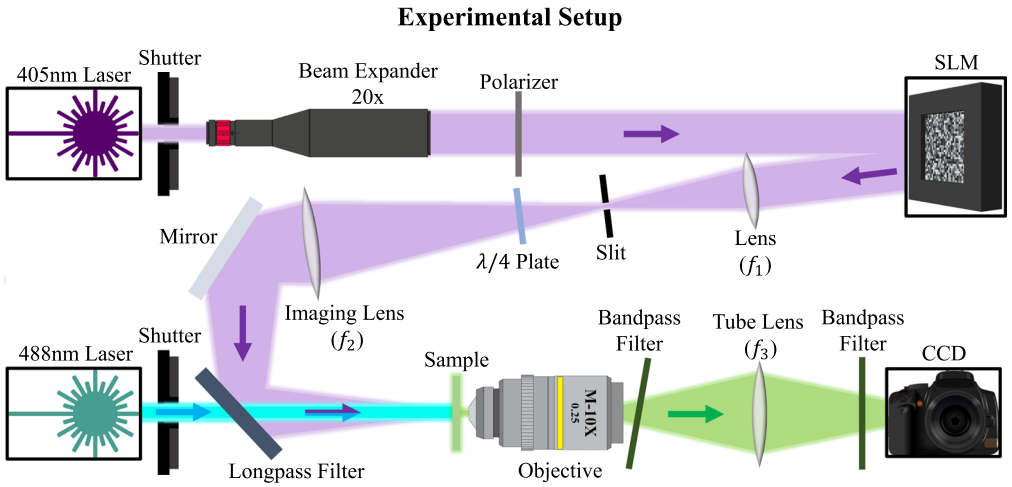

Fig. 1. Experimental setup used for nonlinear speckle-illumination microscopy. We use a phase-only SLM to generate a customized speckle pattern that illuminates and photoconverts a fluorescent sample.

In this work, we introduce and use an ideal family of tailored speckle patterns for nonlinear pattern-illumination microscopy. The speckle patterns we design need to possess the following properties to produce isotropic and uniform super-resolution. All of the vortices in the speckles must have a circular shape and an identical high-intensity halo surrounding each vortex core. Away from the randomly distributed optical vortices, however, the spatial intensity profile of the speckles should be uniform with minor fluctuations. When this is the case, the speckles' intensity PDF is a narrow peak that can be approximated as a delta function. We thus refer to this family of tailored speckles as "delta" speckles. To enable optical sectioning, the delta speckles' field must be fully developed, and as a result, the speckles' intensity pattern will rapidly and non-repeatably evolve upon axial propagation. Experimentally, we generate delta speckle patterns by modulating the phase front of a monochromatic laser beam with a spatial light modulator (SLM). Using delta speckle patterns, we photoconvert a planar fluorescent gel sample and measure the fluorescence signal from the unconverted regions in the vicinity of optical vortices. Not only do we demonstrate a 3× enhanced spatial resolution relative to the optical diffraction limit of the illumination optics, but also we show the significant advantages of using customized speckles over Rayleigh speckles in fluorescence microscopy.

2. EXPERIMENTAL SETUP

In our demonstration, the fluorescent sample is a 25-μm-thick layer of the photoconvertible protein mEos3.2, which is uniformly distributed and suspended in a gel [32] (see the Supplement 1 for details). A continuous-wave (CW) laser beam with a wavelength of $\lambda = 405$ nm is used to photoconvert the protein. The laser's wavefront is modulated by a phase-only SLM, which generates a speckle pattern in its far field (Fourier plane). The polarization of the far-field speckles' field is converted from linear to circular by a quarter-wave plate. The far-field speckle pattern illuminates and photoconverts the sample.

A schematic of the detailed experimental setup for photoconverting a fluorescent sample with customized speckle patterns and imaging the unconverted fluorescence is shown in Fig. 1. The $\lambda = 405$ nm CW laser beam is expanded and linearly polarized before it is incident on the phase-only SLM (Meadowlark Optics). The pixels on the SLM can modulate the phase of the incident field between 0 and 2π: in increments of $2\pi/90$. Because a small portion of light reflected from the SLM is unmodulated, we write a binary phase diffraction grating on the SLM and use the light diffracted to the first order for photoconversion. In order to avoid cross-talk between the neighboring SLM pixels, 32 × 32 pixels are grouped to form one macropixel, and the binary diffraction grating is written within each macropixel with a period of eight pixels. We use a square array of 32 × 32 macropixels in the central part of the phase modulating region of the SLM to shape the photoconverting laser light. The light modulated by our SLM is Fourier transformed by a lens with a focal length of $f_1 = 500$ mm and cropped in the Fourier plane with a slit to keep only the first-order diffraction. The complex field on the Fourier plane of the SLM is imaged onto the surface of the sample by a second lens, with a focal length of $f_2 = 500$ mm. Using a $\lambda/4$ plate, we convert the linearly polarized photoconverting beam into a circularly polarized beam before it is incident upon the sample. In this setup, the full width at half-maximum (FWHM) of a diffraction-limited focal spot is 17 μm.

After the photoconversion process, a second laser, operating at a wavelength of $\lambda = 488$ nm, uniformly illuminates the sample and excites the non-photoconverted mEos3.2 proteins. The unconverted protein fluorescence has a wavelength centered around $\lambda = 532$ nm [32]. To collect the fluorescence, we use a 10× objective of NA = 0.25 and a tube lens with a focal length of $f_3 = 150$ mm. The 2D fluorescence image is recorded by a CCD camera (Allied Vision Manta G-235B). The spatial resolution of the detection system is estimated to be 1.1 μm, which allows us to resolve features in the sample that are smaller than the diffraction limit of our illumination optics. The remaining excitation laser light, which is not absorbed by the sample, is subsequently removed by two Chroma ET 535/70 bandpass filters. One filter is placed after the objective lens and reflects the excitation beam off the optical axis of our system. The second one is placed directly in front of the camera.

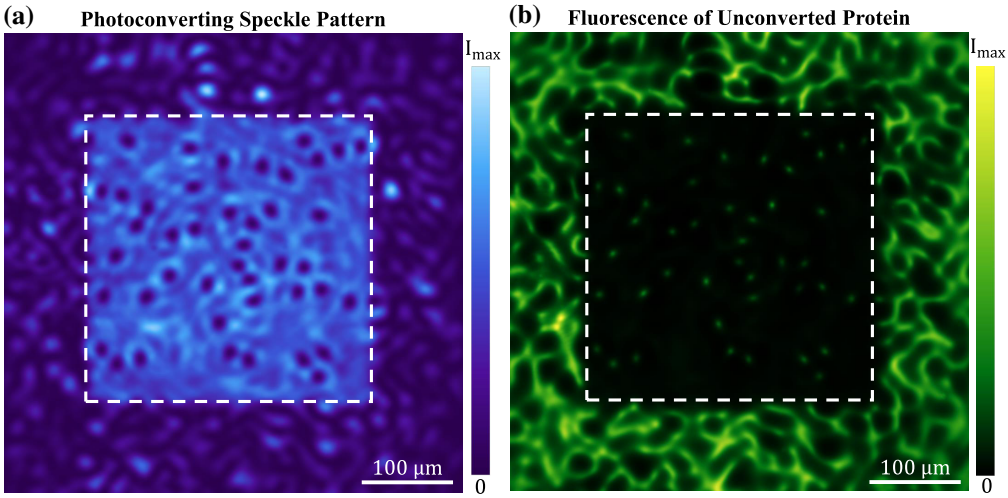

Fig. 2. Customizing speckles for nonlinear pattern illumination. (a) Experimentally recorded speckle pattern that illuminates and photoconverts a uniform fluorescent protein sample. Within the white box, the speckles obey delta statistics, and outside they obey Rayleigh statistics. (b) Experimentally recorded image of the fluorescence from the unconverted regions shows isometric and isotropic spots produced by the vortices in the delta speckles; the region photoconverted by the Rayleigh speckles features large, irregular, and interconnected fluorescent grains.

3. PHOTOCONVERSION FLUORESCENCE MICROSCOPY

Figure 2(a) shows part of an example speckle pattern used to photoconvert the fluorescent sample. The lateral dimension of the entire speckle pattern is 600 μm. The speckle pattern consists of two regions. Within the central region marked by the white dashed square, 300 μm × 300 μm in size, the speckle pattern obeys delta intensity statistics, i.e., a random array of circular vortices embedded in a nearly uniform intensity background. Outside the square, the speckles adhere to Rayleigh statistics, featuring sparse, nearly circular islands of high intensity, randomly distributed in a dark sea. The average speckle grain size is 17 μm. The speckles are created using a modification of the methods presented in Refs. [33–35] (see Supplement 1 for details).

Figure 2(b) shows the fluorescence from the uniform protein gel sample after being photoconverted by the speckle pattern presented in Fig. 2(a). Outside the central square, the sample is photoconverted by the Rayleigh speckle pattern. The fluorescent pattern consists of a sprawling anisotropic web, which reflects the topology of the low-intensity regions surrounding the optical vortices. In stark contrast, the fluorescence pattern within the central square, which is photoconverted by delta speckles, features isolated fluorescent spots of a much smaller size. They are all created by the optical vortices in the central square in Fig. 2(a). The high level of isotropy exhibited by the fluorescent spots originates from the high degree of rotational symmetry that is present in the vortices generating them. Apart from these spots, the fluorescent intensity is uniformly low. This dark background arises from the homogeneity of the delta speckle pattern's intensity away from optical vortices. A qualitative comparison between the distinct fluorescence patterns inside and outside the central square illustrates how customizing the intensity statistics of speckles can significantly enhance the performance of speckle-based pattern illumination microscopy.

Next, in Fig. 3, we quantitatively assess the performance of delta speckles in our application. We compare a diffraction-limited spot, shown in Fig. 3(a), with the fluorescent spots produced in the central region in Fig. 2(b) to quantitatively determine the resolution enhancement. The diffraction-limited spot is created using the experimentally measured field-transmission matrix of the 405 nm light, from the SLM to the sample, and it gives the 2D point spread function (PSF) of our illumination optics. The FWHM of the spot is 17 μm, which is in agreement with the estimated value of 18 μm from the diffraction limit $\lambda/(2\ \mathrm{NA})$, where $\mathrm{NA} \cong 0.011$ is the numerical aperture of the illumination optics. Figure 3(b) shows an example fluorescent spot created by one of the vortices in the illuminating delta speckle pattern. Its shape is close to circular. We determine the FWHM along both the major axis $a = 6.1$ μm and the minor axis $b = 5.0$ μm by fitting (see Supplement 1 for details). The average spot size, $(a + b)/2 \cong 5.6$ μm, is three times below the diffraction limit (17 μm).

To determine the isotropy of the spatial resolution enhancement produced by the delta speckles, we measure the major axis a and minor axis b of all fluorescent spots in the central region. The aspect ratio b/a is a measure of isotropy. Using measurements from a total of 89 fluorescent spots stemming from two independent delta speckle patterns, we calculate a histogram of the ratio (b/a) which is shown in Fig. 3(c). All of the spots are close to circular. The mean value of b/a is 0.86. The most circular fluorescent spot has $b/a = 0.95$, and the least circular spot $b/a = 0.72$.

The size uniformity of the fluorescent spots is reflected in the box-plot analysis of the major and minor axis widths in Fig. 3(d). The mean value of major and minor axis widths, marked by white lines, are $\langle a \rangle = 6.1$ μm and $\langle b \rangle = 5.2$ μm. The black whiskers show the maximum and minimum of the ensemble. The edges of the blue and red shaded regions denote the upper and lower quartiles (25% and 75%) of the data, which are 5.7 μm and 6.4 μm for the major axis a, 4.9 μm and 5.4 μm for the minor axis b. The green dashed line indicates the diffraction limit, i.e., the width of the PSF in (a). Not only do all of the fluorescent spots have a uniform size, but they are also significantly smaller than the diffraction-limited spot size. Therefore, the spatial resolution enhancement provided by delta speckles is homogeneous.

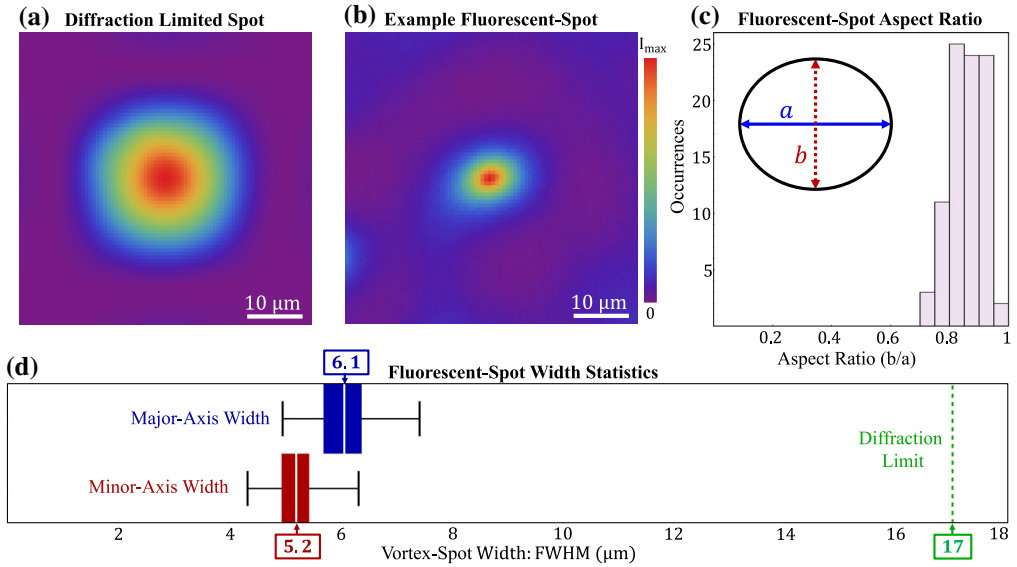

Fig. 3. Circumventing the diffraction limit. (a) Diffraction-limited spot of the 405 nm illumination/photoconversion optics. (b) Example fluorescent spot produced by a vortex in the delta speckle pattern. Its size is much smaller than the diffraction-limited spot. Its shape can be fit by an ellipse of major axis width $a = 6.1$ μm and minor axis width $b = 5$ μm. (c) Aspect ratio, b/a, histogram of all fluorescent spots produced by the delta speckles. The inset illustrates an ellipse with the average aspect ratio $\langle b/a \rangle = 0.86$. (d) Box-plot analysis of the major and minor axes' widths. The white line marks the mean value, and the black whiskers represent the upper and lower bounds of the data. The edges of the blue and red shaded regions mark the upper and lower quartiles (25%, 75%) of the ensemble. The green dashed line indicates the FWHM of the diffraction-limited spot in (a).

4. CUSTOMIZED SPECKLE STATISTICS

In the previous section, we established the significant advantages of creating isotropic and isomeric vortices in the photoconverting speckle patterns used in fluorescence microscopy. Here we characterize the customized speckles' properties in detail and show how their vortex characteristics are transferred to the fluorescent spots. To this end, we use a simpler experimental setup, described in Supplement 1.

An example of an experimentally measured delta speckle pattern is shown in Fig. 4(a). The corresponding 2D phase profile of the speckle pattern is shown in (b). While the 2D intensity profile of the speckle pattern is relatively homogeneous apart from the vortices, the corresponding phase profile is random and irregular everywhere. As shown in Supplement 1, the complex field of the delta speckles adheres to a circular non-Gaussian PDF. The phase has a uniform probability distribution within the range of $-\pi$ to π, and the intensity is independent of the phase; thus, the speckles' field is fully developed.

In Fig. 4(c), we compare the intensity PDF of an ensemble of 100 delta speckle patterns like the one shown in (a) (purple line) to a Rayleigh PDF (green dashed line). Because the Rayleigh intensity PDF exhibits an exponential decay, the most probable intensity values in a Rayleigh speckle pattern are close to zero. Therefore, the spatial profile of a Rayleigh speckle pattern is dominated by the low-intensity regions surrounding the optical vortices. The high-intensity regions, which are the bright speckle grains, are sparse, well separated, and isotropic. In many ways, the spatial profile of a delta speckle pattern is the inverse of a Rayleigh speckle pattern. Because the spatially uniform regions of high intensity dominate the spatial profile of a delta speckle pattern, the intensity PDF is narrowly peaked and centered around the mean value $\langle I \rangle$. The peak's width is a reflection of the intensity fluctuations associated with the speckle grains. The presence of optical vortices, and the surrounding dark regions, in the speckle patterns results in

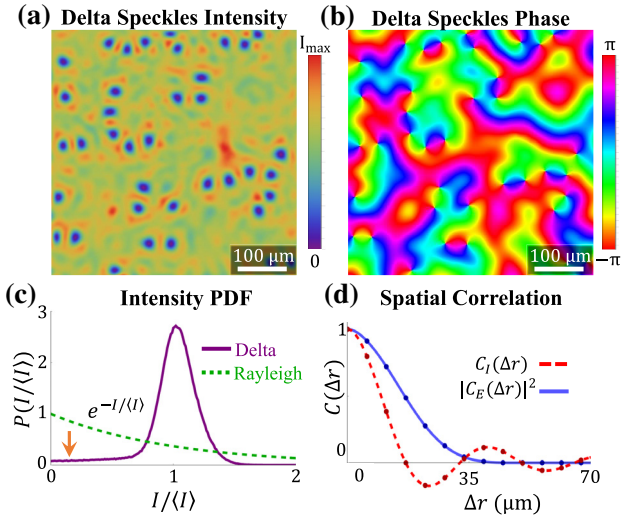

Fig. 4. Customized speckle statistics. (a) Example delta speckle pattern and (b) corresponding phase distribution of its complex field. The phase is randomly distributed between $-\pi$ and π, indicating that the speckle pattern is fully developed. (c) Intensity PDF (purple solid line) of the delta speckle pattern compared with a Rayleigh PDF (green dashed line). (d) Spatial correlation functions of the intensity (red dashed line) and the field (blue solid line) in the delta speckle pattern. The spatial fluctuations of the intensity are faster than those of the field. The anti-correlation ($C_I < 0$) originates from the bright ring surrounding each vortex core. Both plots in (c) and (d) are obtained from an ensemble of 100 speckle patterns.

a low-intensity tail in the PDF extending to $I = 0$ [marked by the orange arrow in (c)]. Because the probability density in this tail is low, the vortices are sparse and spatially isolated.

Using the spatial field correlation function, $C_E(\Delta r)$, and the spatial intensity correlation function, $C_I(\Delta r)$ (see their

definitions in Supplement 1), we can identify the characteristic length scales in a speckle pattern. For a Rayleigh speckle pattern, $C_I(\Delta r) = |C_E(\Delta r)|^2$, and therefore both the field and the intensity fluctuate on the same length scale. The spatial correlation length, defined as the FWHM of $C_I(\Delta r)$, is determined by the diffraction limit. For a delta speckle pattern, $C_I(\Delta r)$ is narrower than $|C_E(\Delta r)|^2$, as can be seen in Fig. 4(d). In the delta speckles, $|C_E(\Delta r)|^2$ remains the same as in Rayleigh speckles, because both patterns are generated by a phase-only SLM, and their spatial frequency spectra are identical. Because $C_I(\Delta r)$ is narrower than $|C_E(\Delta r)|^2$ in a delta speckle pattern, it indicates that the intensity varies faster than the field, spatially. Another difference is that with increasing Δr, the delta speckles' $C_I(\Delta r)$ exhibits a damped oscillation instead of a monotonic decay. These results can be understood as follows: according to the definition of $C_I(\Delta r)$, the features in the speckle patterns that contribute the most to the intensity correlation function are those where the intensity deviates the most from the mean value. In a Rayleigh speckle pattern, the bright speckle grains have the greatest difference in intensity relative to the mean value. As a result, the speckle grain size determines the FWHM of $C_I(\Delta r)$ in a Rayleigh speckle pattern. Conversely, in a delta speckle pattern, the vortices differ from the mean intensity value more than any other element in the pattern. Therefore, the characteristic features of the optical vortices dictate $C_I(\Delta r)$. For example, the high-intensity halo surrounding each vortex core is reflected in the negative correlation $C_I(\Delta r) < 0$ around $\Delta r = 20$ μm, which corresponds to the distance from the vortex center to the high-intensity halo.

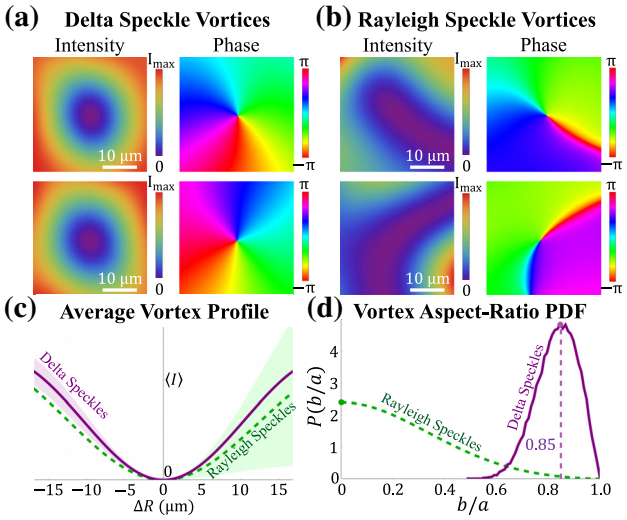

Fig. 5. Optical vortex characteristics. Two example vortices from a (a) delta speckle pattern and (b) Rayleigh speckle pattern. While the vortices in the delta speckles are nearly circular, the Rayleigh speckles' vortices have highly irregular shapes. This property is reflected in (c) where we plot the average intensity profile of light around vortices in 1000 delta speckle patterns (purple solid line) and around vortices in 1000 Rayleigh speckle patterns (green dashed line). The edge of the purple and green shaded regions indicates one standard deviation away from the corresponding mean profile. (d) Probability density of the equal-intensity contours' aspect ratio around the vortices in 1000 delta speckle patterns (purple) next to the theoretical prediction for Rayleigh speckle patterns (green).

5. VORTEX CHARACTERISTICS

In our photoconversion experiment, effectively, the inverse of the $\lambda = 405$ nm speckle pattern is imprinted onto the uniform fluorescent sample. Therefore, after photoconversion, the measured fluorescence originates from the regions of the sample in the vicinity of the optical vortices in the speckle pattern. Here, we investigate the shape and intensity fluctuations of such regions in both delta speckles and Rayleigh speckles. In Figs. 5(a) and 5(b), we magnify two representative vortex-centered regions in a delta speckle pattern and in a Rayleigh speckle pattern. While the dark region surrounding the vortex cores in the delta speckle pattern is relatively circular, it is elongated and irregular in the Rayleigh speckle pattern. These properties are general and occur within one spatial correlation length from the vortex center. In Fig. 5(c), we plot the radial intensity profiles averaged over all vortices in ensembles of delta (purple line) and Rayleigh (green line) speckle patterns. The intensity rises faster with distance from the vortex center in delta speckles, leading to a smaller region of low intensity than found in Rayleigh speckles. In (c), the intensity fluctuations about the average profile are described by the shaded area, whose edges represent one standard deviation from the mean. Relative to Rayleigh speckles, the dramatically reduced intensity fluctuations in the neighborhood of the delta speckles' vortices leads to more consistent vortex profiles.

The core structure of a vortex is characterized by the equal-intensity contour immediately surrounding the phase singularity. As with the fluorescent spots analyzed previously, this structure can be described by an ellipse whose major and minor axis lengths are a and b, respectively. The aspect ratio b/a reflects the degree of isotropy of the vortex core structure. In Fig. 5(d), we plot the PDF of b/a, $P(b/a)$, obtained from 1000 independent delta speckle patterns and compare it with that of Rayleigh speckles. For Rayleigh speckles, $P(b/a)$ has a maximum at $b/a = 0$, indicating the most probable shape of the intensity contour around a vortex is a line [5–7]. Furthermore, the probability of a circular contour, $b/a = 1$, vanishes, confirming the absence of isotropic vortices in a Rayleigh speckle pattern. Contrarily, $P(b/a)$ for the delta speckles features a narrow peak centered at $b/a = 0.85$, meaning all vortices are nearly circular. For comparison, the probability that a vortex will have $b/a > 0.6$ is 99.7% in a delta speckle pattern, while the probability is only 6% in a Rayleigh speckle pattern. Due to the circular symmetry exhibited by the optical vortices [36] in delta speckles, the nearest-neighbor vortex spacing, $\cong 45$ μm, is larger than that in Rayleigh speckles, $\cong 27$ μm. Therefore, the average vortex density is lower in a delta speckle pattern, when compared to a Rayleigh speckle pattern.

6. PROTEIN PHOTOCONVERSION SIMULATION

In this section, we simulate the photoconversion process with a customized speckle pattern. We consider the case of a uniform sample photoconverted by an intensity pattern $I_p(\mathbf{r})$, starting from $t = 0$. The unconverted protein density $\rho(\mathbf{r}, t)$ satisfies the rate equation

$$\frac{d\rho(\mathbf{r}, t)}{dt} = -q I_p(\mathbf{r})\rho(\mathbf{r}, t), \tag{1}$$

where q is a coefficient describing the photoconversion strength. The solution to this equation is given by

$$\rho(\mathbf{r}, t) = \rho_0 e^{-q I_p(\mathbf{r})t}, \tag{2}$$

where $\rho_0 = \rho(\mathbf{r}, 0)$ is the initial uniform protein density.

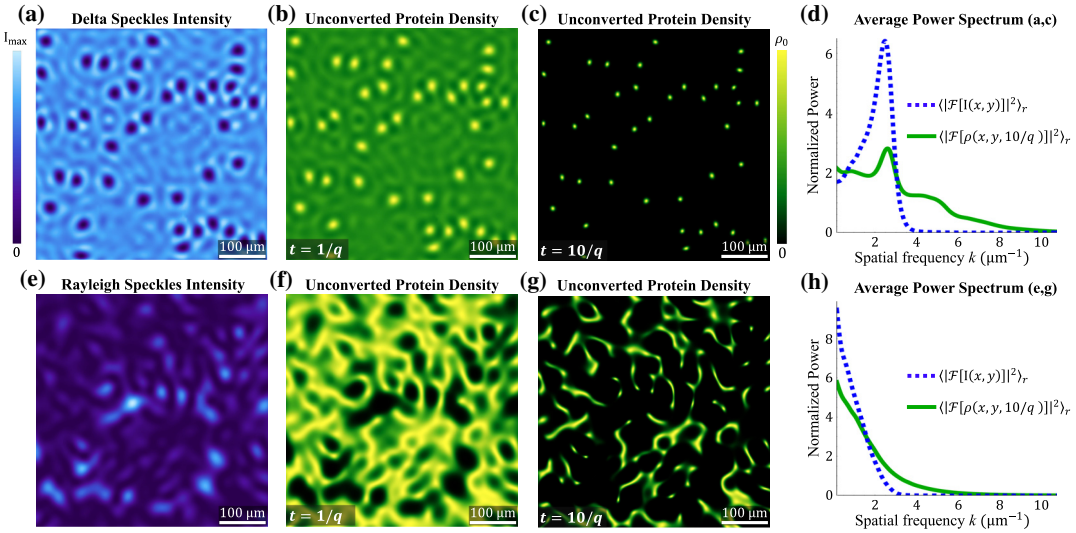

Fig. 6. Photoconversion simulation. (a) When a delta speckle pattern is used for photoconversion, the unconverted regions near the vortices quickly evolve into isotropic and isomeric islands, as seen in (b) at $t = 1/q$. At long timescales, the islands remain, as shown in (c), where $t = 10/q$, yet they have considerably smaller size and higher spatial frequencies, as shown in (d). (e) When a Rayleigh speckle pattern is used for photoconversion, an interconnected web forms instead of isolated islands at $t = 1/q$, as shown in (f). (g) Even at long time scales, isolated and isotropic islands are rarely seen, and fewer high-spatial frequencies are present when compared to (c), as shown in (h). The power spectra in (d), (h) are ensemble averaged over 100 realizations, and normalized to have a mean value of one over the spatial frequencies plotted. Note that the values at $k = 0$ are not plotted.

The fluorescence intensity from the unconverted proteins $I_e(\mathbf{r}, t)$ is proportional to $\rho(\mathbf{r}, t)$. Thus, the negative of the photoconverting intensity $I_p(\mathbf{r}, t)$ is nonlinearly (exponentially) imprinted onto the fluorescence image $I_e(\mathbf{r}, t)$. In Fig. 6, we plot $\rho(\mathbf{r}, t)$ for both delta speckles [Fig. 6(a)] and Rayleigh speckles [Fig. 6(e)]. With increasing photoconversion time, the unconverted regions shrink. As can be seen in Figs. 6(b) and 6(c), for delta speckles, the unconverted regions evolve to isolated circular spots of homogeneous size. For Rayleigh speckles, the unconverted regions have irregular shapes and highly inhomogeneous sizes [Figs. 6(f) and 6(g)]. We compute the power spectra by Fourier transforming the speckled intensity patterns in (a), (e) and the unconverted protein density distributions in (c), (g). The azimuthally averaged power spectra are shown in (d), (h). Because delta speckles possess non-local correlations, which shorten the spatial intensity correlation length, the speckles' intensity power spectrum contains higher spatial frequencies than those present in Rayleigh speckles: which can be seen by comparing the blue dashed lines in (d), (h). As a result, the delta speckles produce higher spatial frequencies in the unconverted protein density patterns, especially at long photoconversion time scales, as shown by green solid lines in (d), (h).

Our model demonstrates that the circularity of the low-intensity region surrounding each vortex in a delta speckle pattern translates directly to the circularity of the corresponding fluorescent spots in the photoconverted sample. This supports our experimental findings, where the aspect ratio of the fluorescent spots has a mean value of $\langle b/a \rangle = 0.86$, which agrees with the mean aspect ratio of the optical vortices, $\langle b/a \rangle = 0.85$. Similarly, this model explains the homogeneity in size and shape of the fluorescent spots when a delta speckle pattern is used for photoconversion. When a Rayleigh speckle pattern is used for photoconversion, the vanishing likelihood of having circular vortices coupled with the irregular shape of the surrounding low intensity regions results in the scarcity of isotropic fluorescent spots.

7. OPTICAL SECTIONING

The rapid axial decorrelation of a speckled intensity pattern, which enables parallel 3D nonlinear patterned-illumination microscopy, is the result of the field's uniform phase distribution. The axial decorrelation length of a speckle pattern is defined as the FWHM of the axial intensity correlation function $C_I(\Delta z)$. For a Rayleigh speckle pattern, the axial decorrelation length R_l is proportional to the Rayleigh range, which is determined by the axial diffraction limit $2\lambda/\mathrm{NA}^2$. With axial propagation, a delta speckle pattern evolves into Rayleigh speckles over one R_l. In Fig. 7(a), an example axial intensity cross-section, $I(x = x_0, y, \Delta z)$, of a delta speckle pattern over one R_l is juxtaposed with a numerical simulation of the corresponding unconverted protein density in a uniform sample, $\rho(x = x_0, y, \Delta z, t = 10/q)$. For comparison, the simulation results for a Rayleigh speckle pattern are shown in (c), (d). As the illuminating speckle patterns decorrelate axially, the fluorescent spots (corresponding to optical vortices) move laterally, enabling parallel 3D nonlinear patterned-illumination microscopy.

As shown in Fig. 7(e), the axial intensity correlation function $C_I(\Delta z)$ of the delta speckles has a notably narrower width than that of the Rayleigh speckles. Consequently, the axial decorrelation length of the delta speckles (FWHM of the axial intensity correlation function) is $R_l/3$, which is three times shorter than that of the Rayleigh speckles. This behavior can be attributed to the rapid axial evolution of a delta speckle pattern into a Rayleigh speckle pattern, a general feature of customized speckles [33–35] (see Supplement 1 for details). However, the axial decorrelation lengths of the unconverted protein density in uniform samples, $\rho(\mathbf{r}, t)$, remains nearly identical for long exposure times [Fig. 7(f)]. This is because the axial decorrelation of $\rho(\mathbf{r}, t)$ is dictated by the lateral movement of optical vortices, when propagating axially, which is almost the same for both families of speckles. Since optical vortices in a delta speckle pattern are farther apart than those in a Rayleigh speckle pattern, their transverse motion is slightly slower, leading to a minor broadening of $C_\rho(\Delta z)$. Nevertheless, the delta speckle

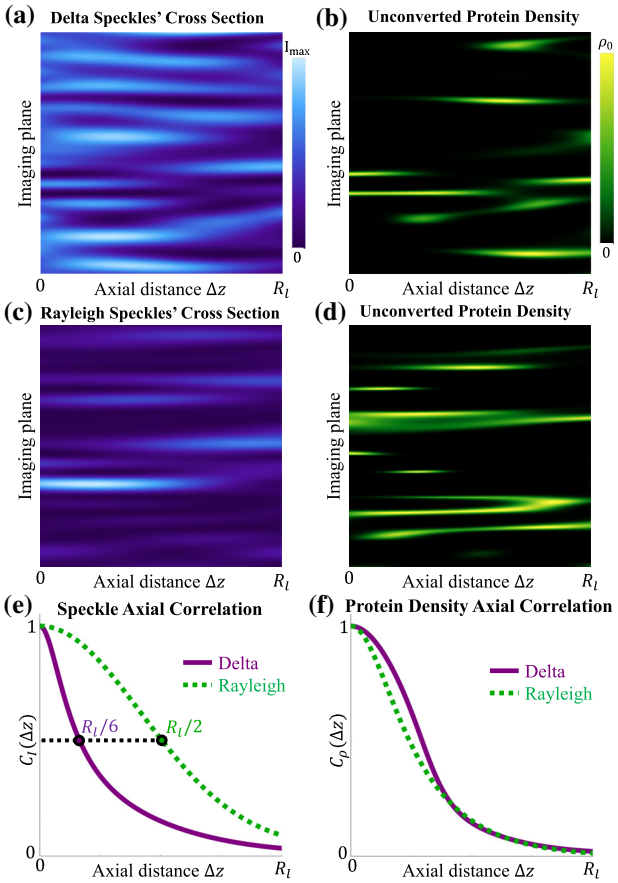

Fig. 7. Axial Propagation. Axial intensity cross-sections, $I(x = x_0, y, \Delta z)$, of both (a) delta and (c) Rayleigh speckles are juxtaposed with a simulation of the corresponding unconverted protein density in a uniform sample, $\rho(x = x_0, y, \Delta z, 10/q)$, (b), (d) over one Rayleigh axial-decorrelation length R_l. (e) The axial intensity correlation function $C_I(\Delta z)$ of the delta speckles (purple line) is three times narrower than that of the Rayleigh speckles (green dashed line). (f) The axial correlation function of the unconverted protein density $C_\rho(\Delta z)$ generated by delta speckles (purple line) has almost the same width as that generated by Rayleigh speckles (green dashed line). We ensemble average over the propagation of 100 speckle patterns to create the curves in (e), (f).

illumination provides approximately the same optical sectioning as the Rayleigh speckle.

8. DISCUSSION AND CONCLUSION

In summary, we have presented a proof-of-principle demonstration of parallel pattern illumination with a family of tailored speckle patterns. By customizing the statistical properties of speckle patterns for photoconversion, we obtain a spatial resolution that is three times higher than the diffraction limit of the illumination optics. The isometric and circular vortices in the tailored speckle patterns provide a homogeneous and isotropic spatial resolution enhancement, which cannot be obtained from standard Rayleigh speckles.

Since the photoconversion process is nonlinear, in principle, there is no limit on the spatial resolution that can be reached. In reality, because the intensity of our photoconverting laser beam is relatively low, the photoconversion process takes a long time (∼12 h). During this time, sample drift and protein motion limit the spatial resolution that can be achieved with fluorescence from the unconverted regions. A further increase in spatial resolution is possible using a higher-powered laser with dilute samples of immobile proteins.

In the photoconversion experiment, the illumination optics has a relatively low NA so that the fluorescence spots of size exceeding 4 μm can be well resolved with the detection optics of 1.1 μm resolution. To reach nanoscale resolution, high-NA optics is required to create the photoconverting speckle pattern. In this case, the vector nature of the light field must be considered. It is known that the axial field at a vortex center can be canceled by manipulating the polarization state of light [37,38]. In a Rayleigh speckle pattern, the intensity contours around a vortex core are elliptical, and the polarization state must be an ellipse with an identical aspect ratio and an identical handedness to cancel the axial field [29,30]. Since the elliptical contours vary in aspect ratio from one vortex to the next in a Rayleigh speckle pattern, it would be challenging, if not impossible, to set the polarization state of a speckle pattern to cancel the axial fields at all of its vortices. In a delta speckle pattern, in contrast, the vortices are almost circular, and half of them have the same handedness. With circularly polarized light, the axial fields will vanish at half of the vortices: specifically, those with the same handedness. To be consistent with high-NA applications, delta speckles with circular polarization are generated in our experiment.

In our experiment, a uniform film of purified protein is photoconverted by a speckle pattern. In Supplement 1, we show that this technique works with live yeast cells, which are nonuniformly distributed in space.

Finally, 2D raster scanning delta speckles over a fluorescent sample enables 3D super-resolution imaging of the sample via the same technique demonstrated with Rayleigh speckles in [30]. Alternatively, it is possible to eliminate scanning from this process by illuminating the entire sample with multiple, distinct, delta speckle patterns that cover the field of view. While the axial resolution obtained using delta speckles for illumination is comparable to that of Rayleigh speckles, further improvements can be made. Specifically, accelerating the transverse motion of optical vortices in delta speckles can enhance their optical sectioning capabilities.

Funding. Office of Naval Research (N00014-20-1-2197); National Science Foundation (DMR-1905465); National Institutes of Health (P30 DK045735); National Institute of General Medical Sciences (R01GM026132, R01GM118486); Wellcome Trust (203285/B/16/Z).

Acknowledgment. We thank Yaron Bromberg for insightful comments. We thank Meadowlark Optics (https://www.meadowlark.com/) for providing the spatial light modulator.

Disclosures. J.B. has financial interests in Bruker Corp. and Hamamatsu Photonics. The remaining co-authors declare no competing interests.

See Supplement 1 for supporting content.

REFERENCES

1. J. C. Dainty, *Laser Speckle and Related Phenomena*, Topics in Applied Physics (Springer, 2013).

2. J. W. Goodman, *Speckle Phenomena in Optics: Theory and Applications* (Roberts and Company, 2007).
3. I. Freund, "'1001' correlations in random wave fields," Waves Random Media **8**, 119–158 (1998).
4. M. Berry and M. Dennis, "Phase singularities in isotropic random waves," Proc. R. Soc. London A **456**, 2059–2079 (2000).
5. M. R. Dennis, "Topological singularities in wave fields," Ph.D. thesis (University of Bristol, 2001).
6. W. Wang, S. G. Hanson, Y. Miyamoto, and M. Takeda, "Experimental investigation of local properties and statistics of optical vortices in random wave fields," Phys. Rev. Lett. **94**, 103902 (2005).
7. S. Zhang and A. Z. Genack, "Statistics of diffusive and localized fields in the vortex core," Phys. Rev. Lett. **99**, 203901 (2007).
8. W. Wang, N. Ishii, Y. Miyamoto, and M. Takeda, "Phase singularities in dynamic speckle fields and their applications to optical metrology," Proc. SPIE **4933**, 175–180 (2003).
9. J. H. Shapiro, "Computational ghost imaging," Phys. Rev. A **78**, 061802 (2008).
10. O. Katz, Y. Bromberg, and Y. Silberberg, "Compressive ghost imaging," Appl. Phys. Lett. **95**, 131110 (2009).
11. Y. Bromberg, O. Katz, and Y. Silberberg, "Ghost imaging with a single detector," Phys. Rev. A **79**, 053840 (2009).
12. C. Ventalon and J. Mertz, "Dynamic speckle illumination microscopy with translated versus randomized speckle patterns," Opt. Express **14**, 7198–7209 (2006).
13. J. Mertz, "Optical sectioning microscopy with planar or structured illumination," Nat. Methods **8**, 811–819 (2011).
14. J. Gateau, T. Chaigne, O. Katz, S. Gigan, and E. Bossy, "Improving visibility in photoacoustic imaging using dynamic speckle illumination," Opt. Lett. **38**, 5188–5191 (2013).
15. E. Mudry, K. Belkebir, J. Girard, J. Savatier, E. Le Moal, C. Nicoletti, M. Allain, and A. Sentenac, "Structured illumination microscopy using unknown speckle patterns," Nat. Photonics **6**, 312–315 (2012).
16. J. Min, J. Jang, D. Keum, S.-W. Ryu, C. Choi, K.-H. Jeong, and J. C. Ye, "Fluorescent microscopy beyond diffraction limits using speckle illumination and joint support recovery," Sci. Rep. **3**, 2075 (2013).
17. J. E. Oh, Y. W. Cho, G. Scarcelli, and Y. H. Kim, "Sub-Rayleigh imaging via speckle illumination," Opt. Lett. **38**, 682–684 (2013).
18. M. Kim, C. Park, C. Rodriguez, Y. Park, and Y. H. Cho, "Superresolution imaging with optical fluctuation using speckle patterns illumination," Sci. Rep. **5**, 16525 (2015).
19. S. Dong, P. Nanda, R. Shiradkar, K. Guo, and G. Zheng, "High-resolution fluorescence imaging via pattern illuminated Fourier ptychography," Opt. Express **22**, 20856–20870 (2014).
20. H. Yılmaz, E. G. van Putten, J. Bertolotti, A. Lagendijk, W. L. Vos, and A. P. Mosk, "Speckle correlation resolution enhancement of wide-field fluorescence imaging," Optica **2**, 424–429 (2015).
21. L. H. Yeh, L. Tian, and L. Waller, "Structured illumination microscopy with unknown patterns and a statistical prior," Biomed. Opt. Express **8**, 695–711 (2017).
22. S. W. Hell and J. Wichmann, "Breaking the diffraction resolution limit by stimulated emission: stimulated-emission-depletion fluorescence microscopy," Opt. Lett. **19**, 780–782 (1994).
23. S. W. Hell, "Far-field optical nanoscopy," Science **316**, 1153–1158 (2007).
24. S. W. Hell and M. Kroug, "Ground-state-depletion fluorescence microscopy: a concept for breaking the diffraction resolution limit," Appl. Phys. B **60**, 495–497 (1995).
25. T. Grotjohann, I. Testa, M. Leutenegger, H. Bock, N. T. Urban, F. Lavoie-Cardinal, K. I. Willig, C. Eggeling, S. Jakobs, and S. W. Hell, "Diffraction-unlimited all-optical imaging and writing with a photochromic GFP," Nature **478**, 204–208 (2011).
26. M. Hofmann, C. Eggeling, S. Jakobs, and S. W. Hell, "Breaking the diffraction barrier in fluorescence microscopy at low light intensities by using reversibly photoswitchable proteins," Proc. Natl. Acad. Sci. USA **102**, 17565–17569 (2005).
27. A. Chmyrov, J. Keller, T. Grotjohann, M. Ratz, E. d'Este, S. Jakobs, C. Eggeling, and S. W. Hell, "Nanoscopy with more than 100,000 'doughnuts,'," Nat. Methods **10**, 737–740 (2013).
28. E. H. Rego, L. Shao, J. J. Macklin, L. Winoto, G. A. Johansson, N. Kamps-Hughes, M. W. Davidson, and M. G. Gustafsson, "Nonlinear structured-illumination microscopy with a photoswitchable protein reveals cellular structures at 50-nm resolution," Proc. Natl. Acad. Sci. USA **109**, E135–E143 (2012).
29. M. Pascucci, G. Tessier, V. Emiliani, and M. Guillon, "Superresolution imaging of optical vortices in a speckle pattern," Phys. Rev. Lett. **116**, 093904 (2016).
30. M. Pascucci, S. Ganesan, O. Tripathi, O. Katz, V. Emiliani, and M. Guillon, "Compressive three-dimensional super-resolution microscopy with speckle-saturated fluorescence excitation," Nat. Commun. **10**, 1327 (2019).
31. N. Meitav, E. N. Ribak, and S. Shoham, "Point spread function estimation from projected speckle illumination," Light Sci. Appl. **5**, e16048 (2016).
32. M. Zhang, H. Chang, Y. Zhang, J. Yu, L. Wu, W. Ji, J. Chen, B. Liu, J. Lu, Y. Liu, J. Zhang, P. Xu, and T. Xu, "Rational design of true monomeric and bright photoactivatable fluorescent proteins," Nat. Methods **9**, 727–729 (2012).
33. N. Bender, H. Yılmaz, Y. Bromberg, and H. Cao, "Creating and controlling complex light," APL Photon. **4**, 110806 (2019).
34. N. Bender, H. Yılmaz, Y. Bromberg, and H. Cao, "Introducing non-local correlations into laser speckles," Opt. Express **27**, 6057–6067 (2019).
35. N. Bender, H. Yılmaz, Y. Bromberg, and H. Cao, "Customizing speckle intensity statistics," Optica **5**, 595–600 (2018).
36. L. de Angelis, "The singular optics of random light: a 2D vectorial investigation," Ph.D. thesis (Delft University of Technology, 2018).
37. X. Hao, C. Kuang, T. Wang, and X. Liu, "Phase encoding for sharper focus of the azimuthally polarized beam," Opt. Lett. **35**, 3928–3930 (2010).
38. S. Galiani, B. Harke, G. Vicidomini, G. Lignani, F. Benfenati, A. Diaspro, and P. Bianchini, "Strategies to maximize the performance of a STED microscope," Opt. Express **20**, 7362–7374 (2012).